


## Semiconducting triferroic multiferroics in van der Waals bilayer lattice

Shuyan Chai<sup>1,2</sup>, Qian Wu,<sup>1</sup> Ting Zhang,<sup>1</sup> Guangping Zhang<sup>2</sup>, Ying Dai,<sup>1,\*</sup> Baibiao Huang,<sup>1</sup> and Yandong Ma<sup>1,†</sup><sup>1</sup>*School of Physics, State Key Laboratory of Crystal Materials, Shandong University, Shandan Street 27, Jinan 250100, China*<sup>2</sup>*School of Physics and Electronics, Shandong Normal University, Jinan 250358, China* (Received 14 March 2024; revised 22 May 2024; accepted 3 July 2024; published 20 August 2024)

Despite great fundamental and technological importance, triferroic multiferroics are still substantially unexplored, especially their semiconducting characteristics. Here, we propose a design principle for achieving semiconducting triferroic multiferroicity in a bilayer lattice by utilizing van der Waals stacking as a perturbation. We further demonstrate this principle in a real material: bilayer  $T'$ -TiBr<sub>2</sub>. Based on first-principles calculations, we show that bilayer  $T'$ -TiBr<sub>2</sub> exhibits semiconducting and antiferromagnetic properties. Additionally, its crystal symmetry gives rise to 120° ferroelasticity, and interlayer charge redistribution leads to an out-of-plane electric polarization, thereby realizing the intriguing semiconducting triferroicity. Furthermore, this system is predicted to possess several extraordinary properties, including ferroelastic control of the magnetization orientation and ferroelectric control of the absolute values of spin-polarization-density distributions.

DOI: [10.1103/PhysRevApplied.22.024052](https://doi.org/10.1103/PhysRevApplied.22.024052)

## I. INTRODUCTION

Multiferroics, which exhibit more than one primary ferroic ordering, have attracted broad interest in recent decades. They not only provide a vigorous platform for discovering fundamental phenomena in condensed-matter physics [1,2], but also have transformative technological potential in nonvolatile memories [3]. There are two essential ingredients for realizing multiferroics. One is time-reversal ( $T$ ) symmetry breaking, which allows for the existence of magnetic order [4]. The other is spatial ( $S$ ) symmetry breaking, which can induce ferroelastic or ferroelectric order [5–10]. As these individual characteristic ferroic orders have different physical origins, integrating them in a single-phase multiferroic material is a particularly challenging task [5,6,11]. For example, magnetic order mainly arises from atoms with partially filled  $d$  or  $f$  orbitals [5,12,13], while ferroelectricity normally requires the presence of empty  $d$  or  $f$  orbitals [14,15]. Additionally, ferroelastic and ferroelectric order necessitates different stringent forms of  $S$ -symmetry-breaking forms, which often lead to their inherent exclusion [16]. Consequently, despite numerous efforts in multiferroic research, the development of single-phase multiferroic materials, especially in two-dimensional (2D) lattices, remains rare to date.

So far, several generations of multiferroics have been theoretically predicated or experimentally confirmed [5,17–21]. Typical examples include (anti)ferromagnetic-ferroelectricity [22–25], (anti)ferromagnetic-ferroelasticity [26], and ferroelasticity-ferroelectricity [16,21,27,28]. Compared to these conventional multiferroics, triferroic multiferroics, in which three ferroic properties [i.e., (anti)ferromagnetic, ferroelastic, and ferroelectric orders] coexist in a single phase, are more desired for both fundamental research and device applications because they could further enhance data-storage density and field-manipulation efficiency [5,6,29]. Though highly valuable, as the conventional multiferroics are rare themselves [15,30,31], triferroic multiferroics are naturally scarce. In this sense, in three-dimensional systems, only the concept of triferroicity is proposed, while its material realization is still absent [23,32]. In addition, only a few studies have reported 2D materials with triferroic multiferroics [5,29,33], almost all of which exhibit *metallic character* (including in Ref. [30]). Actually, *semiconducting* triferroic multiferroics in 2D lattices remain largely unexplored, presenting an outstanding challenge for the future development of 2D multiferroics.

Recently, sliding ferroelectricity in 2D van der Waals crystals was theoretically proposed [34,35] and experimentally confirmed [36,37], wherein appropriate van der Waals stacking could break the inversion symmetry and result in ferroelectricity [29,38]. In this study, we suggest a mechanism for achieving semiconducting triferroic multiferroicity in a bilayer lattice by utilizing van der

\*Contact author: daiy60@sdu.edu.cn, daiy60@sina.com

†Contact author: yandong.ma@sdu.edu.cn

Waals stacking as a perturbation, and we further demonstrate this mechanism in a real material: bilayer  $T'$ -TiBr<sub>2</sub>. It should be noted that WTe<sub>2</sub>, with a similar structure, is synthesized in experiments [39,40]. Based on first-principles calculations, we show that bilayer  $T'$ -TiBr<sub>2</sub> exhibits semiconducting and antiferromagnetic characteristics. Moreover, we show that it possesses 120° ferroelasticity due to its particular crystal symmetry, and it also exhibits out-of-plane electric polarization, resulting from interlayer charge redistribution, thereby generating the long-sought-after semiconducting triferroicity. We further reveal that such a system could display many extraordinary properties, e.g., the ferroelastic control of magnetization and orientation and ferroelectric control of the absolute values of spin-polarization-density distributions,  $\rho$  ( $\rho = \rho_u - \rho_l$ , where  $\rho_u$  and  $\rho_l$  correspond to the spin-charge densities of upper and lower layers, respectively.). These findings open a paradigm for realizing semiconducting triferroic multiferroicity in a 2D lattice.

## II. COMPUTATIONAL METHODS

Our first-principles calculations are performed within density-functional theory (DFT), as implemented in the Vienna *ab initio* simulation package [41]. The exchange-correlation functional is described within the generalized gradient approximation (GGA) in the form of the Perdew-Burke-Ernzerhof functional [42,43]. The cutoff energy is set to 500 eV. Grimme's DFT-D3 method [44] is employed to describe the van der Waals interaction. To describe the strong correlations of Ti 3*d* electrons, the GGA + *U* method is adopted with the effective Hubbard,  $U_{\text{eff}} = 3$  eV [45]. The GGA + *U* method is used in electronic structure and band-structure calculations. The convergence criteria for energy and force are set to  $10^{-5}$  eV and 0.01 eV/Å, respectively. The Brillouin zone is sampled using the Monkhorst-Pack scheme of  $5 \times 3 \times 1$  [46]. A vacuum of about 30 Å is adopted to eliminate interactions between adjacent layers. Following previous works [47,48], dipole-moment correction is employed to evaluate the vertical electric polarization, and the ferroelastic-ferroelectric switching pathway is obtained by using the nudged elastic band (NEB) method [49]. The phonon spectra are calculated based on density-functional perturbation theory using the PHONOPY program [50]. *Ab initio* molecular dynamics (AIMD) simulations are performed with a  $2 \times 2 \times 1$  supercell at 300 K for 1 ps with a time step of 5 fs using the *NVT* ensemble [51].

## III. RESULTS AND DISCUSSION

There is inherent exclusion between different traditional ferroics [5,12–15]. To overcome this challenge, the idea we propose here is to introduce van der Waals stacking as a perturbation to create ferroelectric order, such as sliding ferroelectricity. Sliding ferroelectricity is engineered by

artificially stacking nonpolar 2D materials, wherein electric polarization arises from the subtle interplay between interlayer charge redistribution and ionic displacement [29]. Importantly, unlike traditional ferroelectricity, sliding ferroelectricity eliminates inherent exclusion with magnetism. Moreover, sliding ferroelectricity significantly expands the range of 2D ferroelectrics from a few materials with strict symmetry requirements to a large family of 2D materials, thereby overcoming the limitations posed by the symmetry of ferroelasticity. Based on this concept, we can start with a 2D magnetic semiconductor exhibiting ferroelasticity and then stack two layers together to form a bilayer lattice. By further introducing nonequivalence into the structure using van der Waals stacking as a perturbation to break the balance of charge distribution, electric polarization can be induced. It is worth noting that magnetism and ferroelasticity can exhibit some robustness against such external perturbations. Therefore, the emergence of semiconducting triferroic multiferroics in a 2D lattice can be expected.

One candidate system to demonstrate this mechanism for realizing semiconducting triferroic multiferroics is  $T'$ -TiBr<sub>2</sub>. Bulk  $T'$ -TiBr<sub>2</sub> has been synthesized in experiments [52] and it exhibits a layered structure. Such a layered structure would facilitate the exfoliation of monolayer and bilayer  $T'$ -TiBr<sub>2</sub>. Figure 1(a) illustrates the crystal structure of monolayer  $T'$ -TiBr<sub>2</sub>. It exhibits a tetragonal lattice with the  $P2_1/m$  space group. Each unit cell contains two Ti and four Br atoms. The lattice constants are optimized to be  $a = 3.434$  Å and  $b = 6.218$  Å. As shown in Fig. 1(a), monolayer  $T'$ -TiBr<sub>2</sub> has mirror symmetry,  $M_a$ , and a twofold rotational symmetry axis,  $C_{2a}$ . Considering the fact that  $I = M_a C_{2a}$  or  $C_{2a} M_a$ , it possesses inversion symmetry. For bilayer  $T'$ -TiBr<sub>2</sub> exfoliated from its bulk counterpart, as shown in Fig. 1(d), the lower layer is superimposed onto the upper layer with the operation  $M_c(x, y, 0) \rightarrow (0, b_0, c_0)$ , where  $b_0 = 3.76$  Å and  $c_0 = 6.69$  Å. Apparently, the axis of twofold rotational symmetry vanishes, while the mirror symmetry is preserved. This results in the absence of inversion symmetry in bilayer  $T'$ -TiBr<sub>2</sub>. As we discuss later, this feature gives rise to sliding ferroelectricity. The lattice constants of bilayer  $T'$ -TiBr<sub>2</sub> are optimized to be  $a = 3.415$  Å and  $b = 6.176$  Å. The exfoliation energy of bilayer  $T'$ -TiBr<sub>2</sub> is calculated to be 0.307 J/m<sup>2</sup> (as shown in Fig. S1 within the Supplemental Material) [53], which is comparable with that of graphene (0.37 J/m<sup>2</sup>) [54]. This ensures that bilayer TiBr<sub>2</sub> can readily be exfoliated from the existing bulk via mechanical or liquid exfoliation [55]. Our phonon-spectrum calculations and molecular dynamics simulations show that bilayer  $T'$ -TiBr<sub>2</sub> is both thermally and dynamically stable (for more information, please see Note 1 within the Supplemental Material) [53]. It should be noted that the properties of bilayer systems might depend on the stacking patterns. Therefore, in addition to the stacking pattern corresponding to the bulk, we

also consider other stacking patterns of bilayer  $T'$ -TiBr<sub>2</sub> (see Note 2 within the Supplemental Material) [53]. These patterns, however, are all disadvantageous in energy compared with the one corresponding to the bulk, which is excluded in the following discussion.

The valence electronic configuration of Ti is  $3d^24s^2$ . In bilayer  $T'$ -TiBr<sub>2</sub>, by donating two valence electrons to neighboring Br atoms, two valence electrons are left on the Ti atom, resulting in a valence electronic configuration of  $3d^24s^0$ . As shown in Fig. 1(c), each Ti atom coordinates with six Br atoms, and there are four types of Ti—Br bonds, i.e.,  $l_1$ ,  $l_2$ ,  $l_3$ , and  $l_4$ . This forms a distorted octahedral structure with shared edges. It is known that in an octahedral coordination environment, the  $d$  orbitals would split into  $e_g$  and  $t_{2g}$  orbitals. Considering distortion of the octahedral geometry, the degeneration of  $e_g$  and  $t_{2g}$  orbitals would be slightly deformed, resulting in two groups of roughly degenerate  $d$  orbitals:  $e_g$  ( $d_{x^2-y^2}$ ,  $d_{z^2}$ ) and  $t_{2g}$  ( $d_{xy}$ ,  $d_{xz}$ ,  $d_{yz}$ ), as shown in Fig. 2(a). In this regard, the two remaining valence electrons of the Ti atom will partially occupy the  $t_{2g}$  orbitals, resulting in a magnetic moment of  $2 \mu_B$ . Our first-principles calculations indeed show that bilayer  $T'$ -TiBr<sub>2</sub> is spin polarized. And the magnetic moment is calculated to be  $2.00 \mu_B$  per formula unit, mainly localized on Ti atom ( $1.88 \mu_B$ ).

We then investigate the magnetic ground state of bilayer  $T'$ -TiBr<sub>2</sub>. As shown in Fig. S8(a) within the Supplemental Material, we consider six magnetic configurations [53]. The corresponding results are summarized in Table S1 within the Supplemental Material, from which we can see that AFM-4 is the magnetic ground state of monolayer  $T'$ -TiBr<sub>2</sub> [53]. To further determine interlayer magnetic coupling in bilayer  $T'$ -TiBr<sub>2</sub>, we consider two magnetic configurations with interlayer ferromagnetic coupling and interlayer antiferromagnetic coupling, respectively, as shown in Fig. S8(b) within the Supplemental Material [53].

We find that the interlayer antiferromagnetic configuration is energetically more stable than the ferromagnetic configuration. We come to the conclusion that the antiferromagnetic configuration is energetically more stable than the ferromagnetic configuration. In addition, we also consider the noncollinear magnetic configurations. As shown in Fig. S9 within the Supplemental Material, these noncollinear magnetic configurations have higher energy than the ground-state collinear antiferromagnetic (AFM) state [53]. The Néel temperature is calculated to be 82 K (Note 3 within the Supplemental Material) [53]. Furthermore, we also investigate the magnetic ground configuration of bulk  $T'$ -TiBr<sub>2</sub> by considering different magnetic configurations and find that its magnetic ground state is the same as bilayer  $T'$ -TiBr<sub>2</sub> (Fig. S11 within the Supplemental Material) [53]. Figure 2(b) shows the band structure of bilayer  $T'$ -TiBr<sub>2</sub> in the magnetic ground state. Clearly, it exhibits semiconducting character with an indirect band gap of 0.73 eV, with the valence-band maximum located at the  $X$  point and the conduction-band minimum located at the  $\Gamma$  point. Therefore, bilayer  $T'$ -TiBr<sub>2</sub> is an antiferromagnetic semiconductor.

We also calculate the magnetic anisotropic energy (MAE) of bilayer  $T'$ -TiBr<sub>2</sub> as a function of polar angle  $\Phi$  ( $\theta$ ) in the  $a$ - $b$  ( $b$ - $c$ ) plane. As shown in Figs. 2(c) and 2(d), bilayer  $T'$ -TiBr<sub>2</sub> exhibits significant magnetic anisotropy, and the corresponding most-stable magnetization orientations are the in-plane direction of  $60^\circ$  from the  $a$  axis and the out-of-plane direction along the  $b$  axis, respectively. Furthermore, the former is more stable than the latter, suggesting that the magnetization orientation of bilayer  $T'$ -TiBr<sub>2</sub> prefers the in-plane direction.

By comparing the crystal structure of monolayer  $T'$ -TiBr<sub>2</sub>, we can observe that  $T'$ -TiBr<sub>2</sub> can be evaluated from it through dimerizing two adjacent lines of metal atoms. Such dimerization can occur along three equivalent

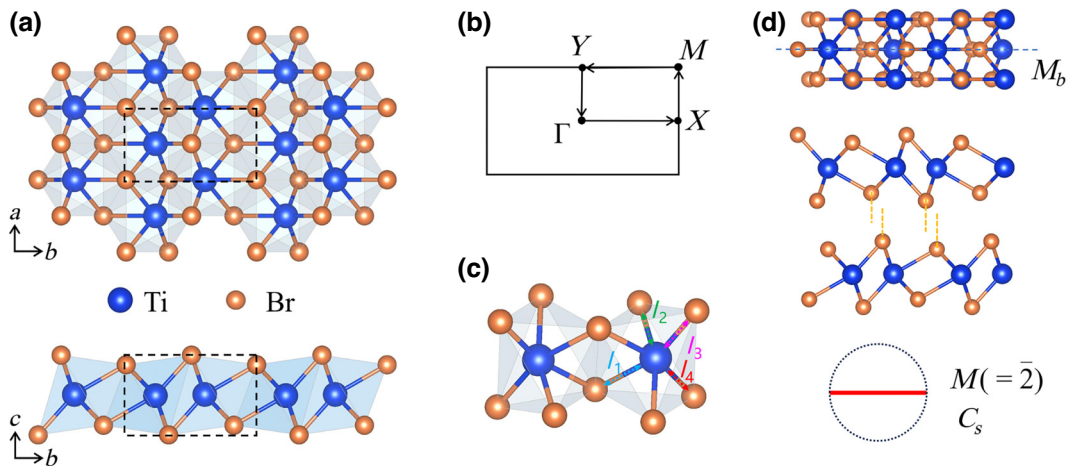


FIG. 1. (a) Crystal structure of monolayer  $T'$ -TiBr<sub>2</sub> from top and side views. (b) 2D Brillouin zone. (c) Distorted octahedral geometry of TiBr<sub>6</sub>. (d) Crystal structure and equatorial plane projections of point groups for bilayer  $T'$ -TiBr<sub>2</sub>.

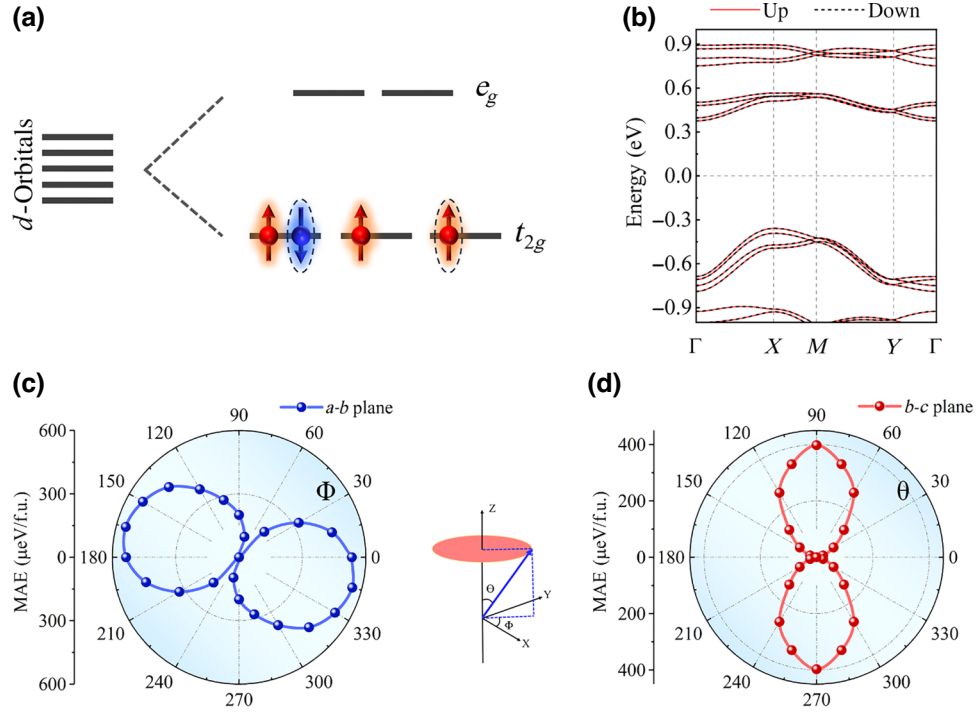


FIG. 2. (a)  $d$ -Orbital splitting of the Ti atom under the distorted octahedral crystal field. (b) Band structure of bilayer  $T'$ -TiBr<sub>2</sub> in the magnetic ground state. Fermi level is set to 0 eV. (c) MAE of bilayer  $T'$ -TiBr<sub>2</sub> with respect to the polar angle in the  $a$ - $b$  plane (in-plane direction of  $60^\circ$  with the  $a$  axis as a reference). (d) MAE of bilayer  $T'$ -TiBr<sub>2</sub> with respect to the polar angle of the  $b$ - $c$  plane ( $b$ -axis direction as a reference).

directions, resulting in three orientation states, i.e.,  $O_1$ ,  $O_2$ , and  $O_3$ . These three orientation states are equivalent in energy, with the lattice rotated by  $120^\circ$  from each other. Obviously, these three orientation states can be considered as three ferroelastic states, which can be transformed into each other without diffusion under external mechanical deformation [29]. Upon forming the bilayer lattice, as shown in Fig. 3(a), the three orientation states are inherited, resulting in  $120^\circ$  ferroelasticity in bilayer  $T'$ -TiBr<sub>2</sub>. To estimate the feasibility of the ferroelastic switch in bilayer  $T'$ -TiBr<sub>2</sub>, we take the transformation from  $O_2$  to  $O_3$  as an example to investigate the ferroelastic transition process. As shown in Fig. 3(b), the intermediate state is the  $T$  phase, and the corresponding ferroelastic phase-transition barrier is calculated to be 43.53 meV/f.u., which corresponds the energy difference between the  $T$  and  $T'$  phases being 43.53 meV/f.u. This value is smaller than those of InOCl (318 meV/f.u.) and InOBr (237 meV/f.u.) [56], and comparable to  $t$ -YN (66 meV/f.u.) [57]. Such a moderate barrier suggests the feasibility of  $120^\circ$  ferroelasticity in bilayer  $T'$ -TiBr<sub>2</sub>.

We also investigate the Young's modulus,  $Y(\theta)$ , and Poisson ratio,  $\nu(\theta)$ , of bilayer  $T'$ -TiBr<sub>2</sub>, which can be obtained using [58]

$$Y(\theta) = \frac{C_{11}C_{22} - C_{12}^2}{C_{11} \sin^4\theta + A \sin^2\theta \cos^2\theta + C_{22} \cos^4\theta},$$

$$\nu(\theta) = \frac{C_{12} \sin^4\theta - B \sin^2\theta \cos^2\theta + C_{12} \cos^4\theta}{C_{11} \sin^4\theta + A \sin^2\theta \cos^2\theta + C_{22} \cos^4\theta}.$$

Here,  $A = (C_{11}C_{22} - C_{12}^2)/C_{44} - 2C_{12}$ ,  $B = C_{11} + C_{22} - (C_{11}C_{22} - C_{12}^2)/C_{44}$ , and  $\theta = 0$  is the direction along the  $a$  axis. As shown in Fig. 3(c),  $Y(\theta)$  of bilayer  $T'$ -TiBr<sub>2</sub> ranges from 118 to 128 N/m, exhibiting mechanical anisotropy. These values are smaller than those of graphene (340 N/m) [59] and BN (318 N/m) [60], indicating the mechanical flexibility of bilayer  $T'$ -TiBr<sub>2</sub> and ensuring the feasibility of the ferroelastic phase transition. The Poisson ratio refers to the negative ratio of transverse strain to longitudinal strain in uniaxial tension or compression. As shown in Fig. 3(d),  $\nu(\theta)$  of bilayer  $T'$ -TiBr<sub>2</sub> varies from 0.13 to 0.15, which is comparable to the Poisson ratios of most two-dimensional materials (0–0.5) [61]. Such a moderate Poisson ratio suggests a sensitive structural response to external stress, which is also beneficial for the ferroelasticity of bilayer  $T'$ -TiBr<sub>2</sub>.

To gain further insights into the ferroelastic properties of bilayer  $T'$ -TiBr<sub>2</sub>, we describe the ferroelastic transition process mathematically using  $2 \times 2$  in-plane-transformation strain matrices. On the basis of lattice vectors and atomic coordinates in Cartesian coordinates, the matrices of  $O_1$ ,  $O_2$ , and  $O_3$  of bilayer  $T'$ -TiBr<sub>2</sub> can be represented by  $H_1 = [6.865, 0; 0, 12.436]$ ,  $H_2 = [7.050, -0.263; 0.001, 11.961]$ , and  $H_3 = [7.050, 0.263; -0.001,$

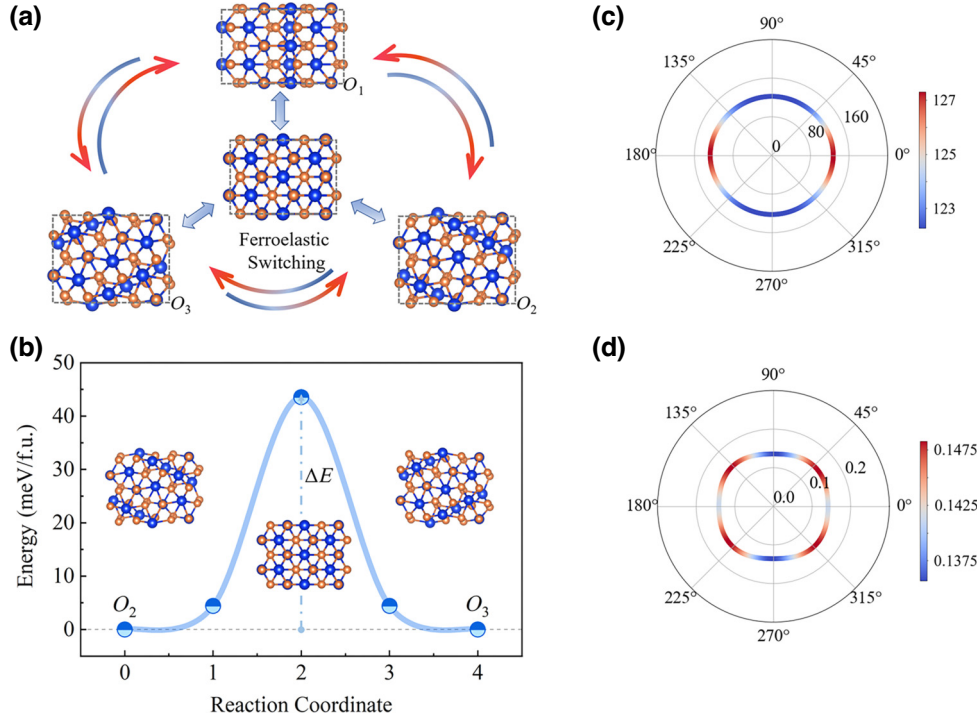


FIG. 3. (a) Interconversion of three ferroelastic states of bilayer  $T'$ -TiBr<sub>2</sub>. (b) Energy changes during the ferroelastic transformation ( $O_2 \rightarrow O_3$ ) of bilayer  $T'$ -TiBr<sub>2</sub>. (c) Young's modulus and (d) Poisson's ratio of bilayer  $T'$ -TiBr<sub>2</sub>.

11.961]. These matrices are linked to each other under the transformation matrix,  $\eta_{ij}$ , namely,  $H_j = \eta_{ij} H_i$ . According to the Green-Lagrange strain tensor, the transformation strain matrix,  $\eta_{ij}$ , can be expressed as [62]

$$\eta_{ij} = \frac{1}{2} ([H_i^{-1}]^T H_j^T H_j H_i^{-1} - I).$$

Here,  $I$  represents the identity matrix.  $\eta_{ij}$  has a symmetric form,  $[\varepsilon_{aa}, \varepsilon_{ab}; \varepsilon_{ab}, \varepsilon_{bb}]$ , wherein the diagonal element,  $\varepsilon_{aa}$  ( $\varepsilon_{bb}$ ), represents the tensile or compressive strain along direction  $a$  ( $b$ ), and the off-diagonal element,  $\varepsilon_{ab}$ , represents the shear-strain component. Taking the  $O_1$  state as a reference, the transition strain matrices in the switching process of  $O_1 \rightarrow O_2$  and  $O_1 \rightarrow O_3$  in bilayer  $T'$ -TiBr<sub>2</sub> can be expressed as

$$\eta_{12(O_1 \rightarrow O_2)} = \begin{pmatrix} 0.055 & -0.022 \\ -0.022 & -0.074 \end{pmatrix},$$

$$\eta_{13(O_1 \rightarrow O_3)} = \begin{pmatrix} 0.055 & 0.022 \\ 0.022 & -0.074 \end{pmatrix}.$$

This suggests that when applying external strain  $\eta_{12}$  ( $\eta_{13}$ ) to  $O_1$ , bilayer  $T'$ -TiBr<sub>2</sub> would be thermodynamically more stable under  $O_2$  ( $O_3$ ).

As mentioned above, under the stacking operation  $M_c(x, y, 0) \rightarrow (0, b_0, c_0)$ , the central inversion symmetry is broken, and the symmetry along the  $c$  direction is reduced.

This leads to inequivalence between the atoms of the upper and lower layers, resulting in the displacement of charge centers in the two layers, thus generating electric polarization along the out-of-plane direction. The electric polarization of bilayer  $T'$ -TiBr<sub>2</sub> is calculated to be  $1.68 \times 10^{-4}$  C/m<sup>2</sup>. To further validate the electric polarization of bilayer  $T'$ -TiBr<sub>2</sub>, we calculate its planar average electrostatic potential. As shown in Fig. 4(d), there is a noticeable energy discontinuity in the vacuum layer, which confirms the existence of out-of-plane electric polarization in bilayer  $T'$ -TiBr<sub>2</sub>. The bilayer lattice with van der Waals stacking exhibits point-group symmetry  $Pm$ , indicating out-of-plane ferroelectricity. In contrast, for the single-layer lattice, the point-group symmetry is  $P2_1/m$ , which features inversion symmetry and results in the absence of ferroelectric polarization.

After identifying the existence of electric polarization, we explore the possibility of reversing its direction. For convenience of discussion, we define the state with electric polarization along the  $c$  direction as state 1 [Fig. S12(a) within the Supplemental Material] [53]. Upon imposing a mirror symmetry operation,  $m_z$ , on state 1, we obtain the alternative configuration of bilayer  $T'$ -TiBr<sub>2</sub>, referred to as state 2 [Fig. S12(b) within the Supplemental Material] [53]. Naturally, state 1 and state 2 are degenerate in energy. Moreover, the opposite displacement of charge centers between the two layers in state 2 compared to state 1 is observed. This indicates that state 2 exhibits a reversed

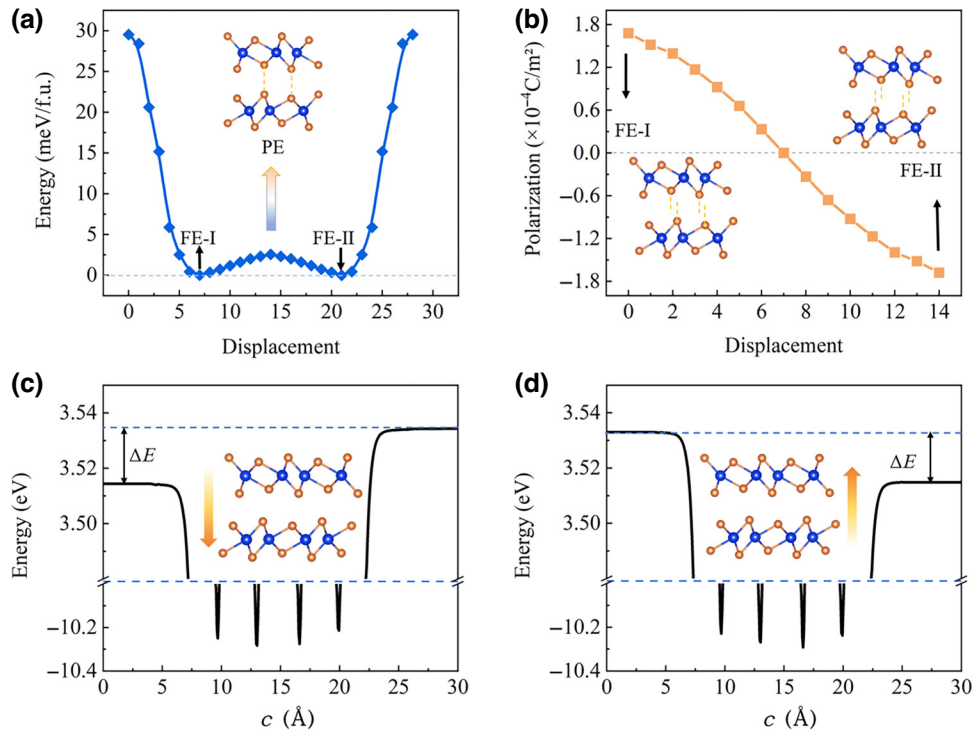


FIG. 4. (a) Ferroelectric phase-transition pathway of bilayer  $T'$ -TiBr<sub>2</sub>. Inset in (a) shows the crystal structure of the intermediate state. (b) Change of the electric polarization value of bilayer  $T'$ -TiBr<sub>2</sub> during the ferroelectric phase transition. Insets in (b) display the crystal structures of ferroelectric state 1 and state 2. Planar average electrostatic potential of (c) ferroelectric state 2 and (d) ferroelectric state 1, where yellow arrows indicate the directions of electric polarization.

electric polarization of  $-1.68 \times 10^{-4}$  C/m<sup>2</sup>, which is further confirmed by the reversed energy discontinuity in planar average electrostatic potential shown in Fig. 4(c). In principle, these two states can be converted into each other via interlayer sliding. In this case, state 1 and state 2 can be regarded as two ferroelectric states.

To assess the feasibility of the ferroelectric phase transition in bilayer  $T'$ -TiBr<sub>2</sub>, we investigate the ferroelectric polarization-switching pathway using the NEB method. The configuration with the  $C_{2v}$  point group is set as the intermediate state [as shown in the inset of Fig. 4(a)], wherein the out-of-plane electric polarization is eliminated. Fig. S2(c) within the Supplemental Material displays the phonon spectra of the intermediate state [53]. It can be observed that there are some negative values in the spectra, indicating that the material would spontaneously transition into state 1 or state 2. The ferroelectric phase-transition barrier of bilayer  $T'$ -TiBr<sub>2</sub> is calculated to be 2.56 meV/f.u. [Fig. 4(a)], which is lower than that of  $T'$ -VTe<sub>2</sub> (10 meV/f.u.) [29] and perovskite ferroelectric BaTiO<sub>3</sub> (200 meV/f.u.) [63], but higher than that of  $T'$ -ZrI<sub>2</sub> (1.6 meV/f.u.) [64]. This confirms that the ferroelectric phase transition in bilayer  $T'$ -TiBr<sub>2</sub> is feasible. The corresponding change of electric polarization during ferroelectric state switching is shown in Fig. 4(b). Therefore, in addition to antiferromagnetic and ferroelastic orders,

bilayer  $T'$ -TiBr<sub>2</sub> also exhibits sliding ferroelectricity, thus achieving the intriguing semiconducting triferroicity.

In addition to the bilayer system, we also investigated the triferroicity properties in trilayer  $T'$ -TiBr<sub>2</sub> (Note 4 within the Supplemental Material) [53]. It is interesting to note that, similar to bilayer  $T'$ -TiBr<sub>2</sub>, antiferromagnetism and ferroelasticity can be inherited from the monolayer. However, due to the cancelation of electric polarization from the two interfaces, the electric polarization value is calculated to be only  $2.575 \times 10^{-6}$  C/m<sup>2</sup>, which is significantly smaller than that of bilayer  $T'$ -TiBr<sub>2</sub>.

Such triferroic multiferroics realized in bilayer  $T'$ -TiBr<sub>2</sub> can result in many intriguing physical phenomena. For example, bilayer  $T'$ -TiBr<sub>2</sub> displays magnetic anisotropy, with the magnetization orientation preferring the in-plane direction of 60° from the  $a$  axis. In other words, the magnetization orientation of bilayer  $T'$ -TiBr<sub>2</sub> is dependent on the lattice structure. It should be noted that the lattice orientations can be switched during the ferroelastic phase transition. Therefore, the magnetization orientation can be effectively controlled by ferroelasticity, indicating a strong magnetism-ferroelasticity coupling effect in bilayer  $T'$ -TiBr<sub>2</sub>. In addition to ferroelasticity, the magnetic properties of bilayer  $T'$ -TiBr<sub>2</sub> can also couple with its ferroelectricity. Because of the existence of ferroelectric polarization along the out-of-plane direction, the

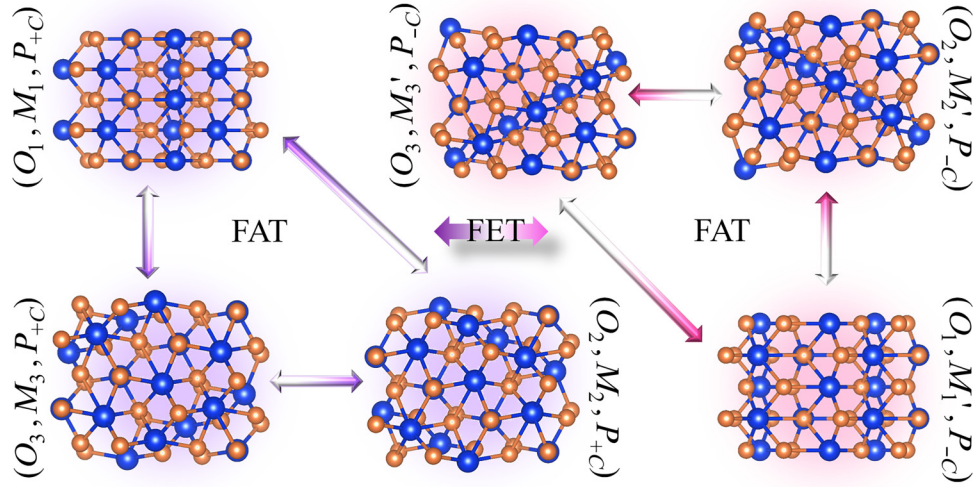


FIG. 5. Diagram of switching among six states in bilayer  $T'$ -TiBr<sub>2</sub> under ferroelastic and ferroelectric phase transitions. Arrows represent transitions between different states.

absolute values of spin-polarization-density distributions on the two layers of bilayer  $T'$ -TiBr<sub>2</sub> are different. Upon switching the ferroelectric polarization, the absolute values of spin-polarization-density distributions in the two layers are also reversed. Hence, the magnetism and ferroelectricity are strongly coupled in bilayer  $T'$ -TiBr<sub>2</sub>, resulting in compelling magnetoelectric coupling within the 2D lattice.

In view of the coexistence of these primary ferroic orders, it is feasible to achieve six-state storage in bilayer  $T'$ -TiBr<sub>2</sub>, as illustrated in Fig. 5. Concerning ferroelectric state 1, there are three ferroelastic states (i.e.,  $O_1$ ,  $O_2$ , and  $O_3$ ) generated by the ferroelastic phase transition, which correspond to three kinds of antiferromagnetic states with different magnetization orientations. These three kinds of states can be converted into each other via ferroelastic transitions (FATs). Akin to ferroelectric state 1, ferroelectric state 2 is also associated with three such states (i.e.,  $O_1$ ,  $O_2$ , and  $O_3$ ). The switching between the two ferroelectric states can be achieved through interlayer sliding. Consequently, six logical states are realized in bilayer  $T'$ -TiBr<sub>2</sub>, which can be transformed into each other through ferroelastic and ferroelectric transitions (FETs) [Fig. 5]. Here, we refer to ferroelectric state 1 and state 2 as  $P_{+c}$  and  $P_{-c}$ , respectively, and we denote the three antiferromagnetic states corresponding to the three ferroelastic states (i.e.,  $O_1$ ,  $O_2$ , and  $O_3$ ) in ferroelectric state 1 (2) as  $M_1$  ( $M_1'$ ),  $M_2$  ( $M_2'$ ), and  $M_3$  ( $M_3'$ ), respectively. In this regard, the corresponding six logical states can be denoted as  $(O_1, M_1, P_{+c})$ ,  $(O_2, M_2, P_{+c})$ ,  $(O_3, M_3, P_{+c})$ ,  $(O_1, M_1', P_{-c})$ ,  $(O_2, M_2', P_{-c})$ , and  $(O_3, M_3', P_{-c})$  respectively. The switching among these states is illustrated in Fig. 5. Considering the coupling effect between them, the six logical states can be directly measured by measuring

the ferroelectric and antiferromagnetic behaviors [21,31]. In detail, concerning the ferroelectric behaviors, piezoresponse force microscopy can be employed [65,66], while, for the antiferromagnetic spin axis, it can be detected using x-ray magnetic linear dichroism spectroscopy [67,68].

#### IV. CONCLUSION

We propose a mechanism to achieve semiconducting triferroic multiferroicity in a bilayer lattice through employing van der Waals stacking as a perturbation. Using first-principles calculations, we further demonstrate it in a real material: bilayer  $T'$ -TiBr<sub>2</sub>. We observe that bilayer  $T'$ -TiBr<sub>2</sub> exhibits semiconducting and antiferromagnetic properties, presents 120° ferroelasticity, and possesses out-of-plane electric polarization, resulting in tantalizing semiconducting triferroicity. Furthermore, we reveal that such a system shows intriguing physics, such as ferroelastic control of magnetization and orientation, as well as ferroelectric control of the absolute values of spin-polarization-density distributions. We hope to further discover more candidate systems in the future and strongly advocate for experimental efforts in the field of semiconducting triferroic multiferroicity.

#### ACKNOWLEDGMENTS

This work is supported by the National Natural Science Foundation of China (Grants No. 12274261 and No. 12074217), the Taishan Young Scholar Program of Shandong Province, and the Shandong Provincial QingChuang Technology Support Plan (Grant No. 2021KJ002).

The authors declare no conflict of interest.

- [1] S. Seki, X. Z. Yu, S. Ishiwata, and Y. Tokura, Observation of skyrmions in a multiferroic material, *Science* **336**, 198 (2012).
- [2] Y. Takahashi, R. Shimano, Y. Kaneko, H. Murakawa, and Y. Tokura, Magnetoelectric resonance with electromagnons in a perovskite helimagnet, *Nat. Phys.* **8**, 121 (2012).
- [3] N. A. Spaldin and R. Ramesh, Advances in magnetoelectric multiferroics, *Nat. Mater.* **18**, 203 (2019).
- [4] C. Zhang, P. Guo, and J. Zhou, Tailoring bulk photovoltaic effects in magnetic sliding ferroelectric materials, *Nano Lett.* **22**, 9297 (2022).
- [5] S. Shen, X. Xu, B. Huang, L. Kou, Y. Dai, and Y. Ma, Intrinsic triferroicity in a two-dimensional lattice, *Phys. Rev. B* **103**, 144101 (2021).
- [6] X. Tang and L. Kou, Two-dimensional ferroics and multiferroics: Platforms for new physics and applications, *J. Phys. Chem. Lett.* **10**, 6634 (2019).
- [7] C. Gong, E. M. Kim, Y. Wang, G. Lee, and X. Zhang, Multiferroicity in atomic van der Waals heterostructures, *Nat. Commun.* **10**, 2657 (2019).
- [8] X. Mu, Y. Pan, and J. Zhou, Pure bulk orbital and spin photocurrent in two-dimensional ferroelectric materials, *npj Comput. Mater.* **7**, 61 (2021).
- [9] S. Liu, I. Grinberg, and A. M. Rappe, Intrinsic ferroelectric switching from first principles, *Nature* **534**, 360 (2016).
- [10] J. Shang, S. Shen, L. Wang, Y. Ma, T. Liao, Y. Gu, and L. Kou, Stacking-dependent interlayer ferroelectric coupling and Moiré domains in a twisted AgBiP<sub>2</sub>Se<sub>6</sub> bilayer, *J. Phys. Chem. Lett.* **13**, 2027 (2022).
- [11] L. Zhang, C. Tang, S. Sanvito, and A. Du, Highly degenerate 2D ferroelectricity in pore decorated covalent/metal organic frameworks, *Mater. Horiz.* **10**, 2599 (2023).
- [12] Z. Gao, F. Ma, X. Zhang, Z. Tian, Y. Liu, Y. Jiao, and A. Du, Predicting MnB<sub>6</sub> monolayer with room temperature ferromagnetism and high magnetic anisotropy, *Phys. E* **134**, 114930 (2021).
- [13] C. Gong, L. Li, Z. Li, H. Ji, A. Stern, Y. Xia, T. Cao, W. Bao, C. Wang, Y. Wang, Z. Q. Qiu, R. J. Cava, S. G. Louie, J. Xia, and X. Zhang, Discovery of intrinsic ferromagnetism in two-dimensional van der Waals crystals, *Nature* **546**, 265 (2017).
- [14] N. Hill, Why are there so few magnetic ferroelectrics?, *J. Phys. Chem. B* **104**, 6694 (2000).
- [15] H. Tan, M. Li, H. Liu, Z. Liu, Y. Li, and W. Duan, Two-dimensional ferromagnetic-ferroelectric multiferroics in violation of the  $d^0$  rule, *Phys. Rev. B* **99**, 195434 (2019).
- [16] H. Wang and X. Qian, Two-dimensional multiferroics in monolayer group IV monochalcogenides, *2D Mater.* **4**, 015042 (2017).
- [17] N. A. Spaldin and M. Fiebig, The renaissance of magnetoelectric multiferroics, *Science* **309**, 391 (2005).
- [18] N. Ding, J. Chen, S. Dong, and A. Stroppa, Ferroelectricity and ferromagnetism in a VOI<sub>2</sub> monolayer: Role of the Dzyaloshinskii-Moriya interaction, *Phys. Rev. B* **102**, 165129 (2020).
- [19] J.-J. Zhang, L.-F. Lin, Y. Zhang, M. Wu, B. Yakobson, and S. Dong, Type-II multiferroic Hf<sub>2</sub>VC<sub>2</sub>F<sub>2</sub> MXene monolayer with high transition temperature, *J. Am. Chem. Soc.* **140**, 9768 (2018).
- [20] X. Xu, Y. Ma, T. Zhang, C. Lei, B. Huang, and Y. Dai, Prediction of two-dimensional antiferromagnetic ferroelasticity in an AgF<sub>2</sub> monolayer, *Nanoscale Horiz.* **5**, 1386 (2020).
- [21] H. Wang, X. Li, J. Sun, Z. Liu, and J. Yang, BP<sub>5</sub> monolayer with multiferroicity and negative Poisson's ratio: A prediction by global optimization method, *2D Mater.* **4**, 045020 (2017).
- [22] J. Chauleau, T. Chirac, S. Fusil, V. Garcia, W. Akhtar, J. Tranchida, P. Thibaudeau, I. Gross, C. Blouzon, A. Finco, M. Bibes, B. Dkhil, D. D. Khalyavin, P. Manuel, V. Jacques, N. Jaouen, and M. Viret, Electric and antiferromagnetic chiral textures at multiferroic domain walls, *Nat. Mater.* **19**, 386 (2020).
- [23] W. Eerenstein, N. D. Mathur, and J. F. Scott, Multiferroic and magnetoelectric materials, *Nature* **442**, 759 (2006).
- [24] J.-M. Hu, T. Nan, N. X. Sun, and L.-Q. Chen, Multiferroic magnetoelectric nanostructures for novel device applications, *MRS Bull.* **40**, 728 (2015).
- [25] Z. Tu, M. Wu, and X. C. Zeng, Two-dimensional metal-free organic multiferroic material for design of multifunctional integrated circuits, *J. Phys. Chem. Lett.* **8**, 1973 (2017).
- [26] L. Seixas, A. Rodin, A. Carvalho, and A. H. Castro Neto, Multiferroic two-dimensional materials, *Phys. Rev. Lett.* **116**, 206803 (2016).
- [27] Y. Gao, M. Wu, and X. C. Zeng, Phase transitions and ferroelasticity–multiferroicity in bulk and two-dimensional silver and copper monohalides, *Nanoscale Horiz.* **4**, 1106 (2019).
- [28] S.-H. Zhang and B.-G. Liu, A controllable robust multiferroic GaTeCl monolayer with colossal 2D ferroelectricity and desirable multifunctionality, *Nanoscale* **10**, 5990 (2018).
- [29] T. Zhang, X. Xu, Y. Dai, B. Huang, and Y. Ma, Intrinsic ferromagnetic triferroicity in bilayer T'-VTe<sub>2</sub>, *Appl. Phys. Lett.* **120**, 192903 (2022).
- [30] J. Qi, H. Wang, X. Chen, and X. Qian, Two-dimensional multiferroic semiconductors with coexisting ferroelectricity and ferromagnetism, *Appl. Phys. Lett.* **113**, 043102 (2018).
- [31] M. Wu and X. Zeng, Intrinsic ferroelasticity and/or multiferroicity in two-dimensional phosphorene and phosphorene analogues, *Nano Lett.* **16**, 3236 (2016).
- [32] C. Xu, L. B. Wang, Z. B. Liu, L. Chen, J. K. Guo, N. Kang, X. L. Ma, H. M. Cheng, and W. Ren, Large-area high-quality 2D ultrathin Mo<sub>2</sub>C superconducting crystals, *Nat. Mater.* **14**, 1135 (2015).
- [33] X. Feng, X. Ma, L. Sun, J. Liu, and M. Zhao, Tunable ferroelectricity and antiferromagnetism via ferroelastic switching in an FeOOH monolayer, *J. Mater. Chem. C* **8**, 13982 (2020).
- [34] L. Li and M. Wu, Two-dimensional ferroelectrics, multiferroics, and nanogenerators, *ACS Nano* **11**, 6382 (2017).
- [35] T.-T. Zhong, Y. Gao, Y. Ren, and M. Wu, Theoretical designs of low-barrier ferroelectricity, *WIREs Comput. Mol. Sci.* **13**, 1682 (2023).
- [36] M. V. Stern, Y. Waschitz, W. Cao, I. Nevo, K. Watanabe, T. Taniguchi, E. Sela, M. Urbakh, O. Hod, and M. B. Shalom, Interfacial ferroelectricity by van der Waals sliding, *Science* **372**, 1462 (2021).



- [37] M. Wu, Two-dimensional van der Waals ferroelectrics: Scientific and technological opportunities, *ACS Nano* **15**, 9229 (2021).
- [38] T. Zhang, X. L. Xu, B. B. Huang, Y. Dai, and Y. D. Ma, 2D spontaneous valley polarization from inversion symmetric single-layer lattices, *npj Comput. Mater.* **8**, 1481 (2022).
- [39] P. Sharma, F.-X. Xiang, D.-F. Shao, D. Zhang, E. Y. Tsympal, A. R. Hamilton, and J. Seidel, A room-temperature ferroelectric semimetal, *Sci. Adv.* **5**, 5080 (2019).
- [40] Z. Fei, W. Zhao, T. A. Palomaki, B. Sun, M. K. Miller, Z. Zhao, J. Yan, X. Xu, and D. H. Cobden, Ferroelectric switching of a two-dimensional metal, *Nature* **560**, 336 (2018).
- [41] G. Kresse and J. Furthmüller, Efficient iterative schemes for *ab initio* total-energy calculations using a plane-wave basis set, *Phys. Rev. B* **54**, 11169 (1996).
- [42] J. Perdew, K. Burke, and M. Ernzerhof, Generalized gradient approximation made simple, *Phys. Rev. Lett.* **77**, 3865 (1996).
- [43] G. Kresse and D. Joubert, From ultrasoft pseudopotentials to the projector augmented-wave method, *Phys. Rev. B* **59**, 1758 (1999).
- [44] S. Grimme, J. Antony, S. Ehrlich, and S. Krieg, A consistent and accurate *ab initio* parametrization of density functional dispersion correction (DFT-D) for the 94 elements H-Pu, *J. Chem. Phys.* **132**, 154104 (2010).
- [45] V. I. Anisimov, F. Aryasetiawan, and A. I. Lichtenstein, First-principles calculations of the electronic structure and spectra of strongly correlated systems: The LDA+*U* method, *J. Phys.: Condens. Matter.* **9**, 767 (1997).
- [46] J. D. Pack and H. J. Monkhorst, “Special points for Brillouin-zone integrations”—a reply, *Phys. Rev. B* **16**, 1748 (1977).
- [47] T. Zhong, X. Li, M. Wu, and J. M. Liu, Room-temperature multiferroicity and diversified magnetoelectric couplings in 2D materials, *Natl. Sci. Rev.* **7**, 373 (2019).
- [48] Q. Yang, M. Wu, and J. Li, Origin of two-dimensional vertical ferroelectricity in  $\text{WTe}_2$  bilayer and multilayer, *J. Phys. Chem. Lett.* **9**, 7160 (2018).
- [49] G. Mills, H. Jónsson, and G. K. Schenter, Reversible work transition state theory: Application to dissociative adsorption of hydrogen, *Surf. Sci.* **324**, 305 (1995).
- [50] X. Gonze and C. Lee, Dynamical matrices, Born effective charges, dielectric permittivity tensors, and interatomic force constants from density-functional perturbation theory, *Phys. Rev. B* **55**, 10355 (1997).
- [51] R. Barnett and U. Landman, Born-Oppenheimer molecular-dynamics simulations of finite systems: Structure and dynamics of  $(\text{H}_2\text{O})_2$ , *Phys. Rev. B* **48**, 2081 (1993).
- [52] J. A. Wilson, C. Maule, P. Strange, and J. N. Tothill, Anomalous behaviour in the layer halides and oxyhalides of titanium and vanadium: A study of materials close to delocalization, *J. Phys. C: Solid State Phys.* **20**, 4159 (1987).
- [53] See the Supplemental Material at <http://link.aps.org/supplemental/10.1103/PhysRevApplied.22.024052> for the cleavage energy of bilayer  $T'$ - $\text{TiBr}_2$ ; AIMD simulation results of bilayer  $T'$ - $\text{TiBr}_2$ ; phonon spectra of the ferroelectric state and intermediate-state bilayer  $T'$ - $\text{TiBr}_2$ ; different stacking patterns and magnetic configurations of bilayer  $T'$ - $\text{TiBr}_2$ ; different magnetic configurations used to obtain the magnetic ground states of monolayer and bilayer  $T'$ - $\text{TiBr}_2$ ; energy differences of different magnetic configurations of monolayer  $T'$ - $\text{TiBr}_2$ ; the Néel temperature, crystal structure, and different magnetic configurations of bulk  $T'$ - $\text{TiBr}_2$ ; crystal structures of ferroelectric state 1 and state 2; and triferroicity in trilayer  $T'$ - $\text{TiBr}_2$ .
- [54] T. Björkman, A. Gulans, A. V. Krasheninnikov, and R. M. Nieminen, van der Waals bonding in layered compounds from advanced density-functional first-principles calculations, *Phys. Rev. Lett.* **108**, 235502 (2012).
- [55] M. Qiao, J. Liu, Y. Wang, Y. Li, and Z. Chen,  $\text{PdSeO}_3$  monolayer: Promising inorganic 2D photocatalyst for direct overall water splitting without using sacrificial reagents and cocatalysts, *J. Am. Chem. Soc.* **140**, 12256 (2018).
- [56] X. Xu, Y. Ma, B. Huang, and Y. Dai, Two-dimensional ferroelastic semiconductors in single-layer indium oxygen halide  $\text{InOY}$  ( $Y = \text{Cl}/\text{Br}$ ), *Phys. Chem. Chem. Phys.* **21**, 7440 (2019).
- [57] B. Xu, H. Xiang, J. Yin, Y. Xia, and Z. Liu, A two-dimensional tetragonal yttrium nitride monolayer: A ferroelastic semiconductor with switchable anisotropic properties, *Nanoscale* **10**, 215 (2018).
- [58] E. Cadelano, P. L. Palla, S. Giordano, and L. Colombo, Elastic properties of hydrogenated graphene, *Phys. Rev. B* **82**, 235414 (2010).
- [59] R. C. Andrew, R. E. Mapasha, A. M. Ukpogon, and N. Chetty, Mechanical properties of graphene and boronitrene, *Phys. Rev. B* **85**, 125428 (2012).
- [60] K. H. Michel and B. Verberck, Theory of elastic and piezoelectric effects in two-dimensional hexagonal boron nitride, *Phys. Rev. B* **80**, 224301 (2009).
- [61] Z. Gao, X. Dong, N. Li, and J. Ren, Novel two-dimensional silicon dioxide with in-plane negative Poisson’s ratio, *Nano Lett.* **17**, 772 (2017).
- [62] W. Li and J. Li, Ferroelasticity and domain physics in two-dimensional transition metal dichalcogenide monolayers, *Nat. Commun.* **7**, 10843 (2016).
- [63] E. C. Ronald, Origin of ferroelectricity in perovskite oxides, *Nature* **358**, 136 (1992).
- [64] T. Zhang, Y. Liang, X. Xu, B. Huang, Y. Dai, and Y. Ma, Ferroelastic-ferroelectric multiferroics in a bilayer lattice, *Phys. Rev. B* **103**, 165420 (2021).
- [65] D. Zhang, P. Schoenherr, P. Sharma, and J. Seidel, Ferroelectric order in van der Waals layered materials, *Nat. Rev. Mater.* **8**, 25 (2023).
- [66] D. Lebeugle, D. Colson, A. Forget, M. Viret, P. Bonville, J. F. Marucco, and S. Fusil, Room-temperature coexistence of large electric polarization and magnetic order in  $\text{BiFeO}_3$  single crystals, *Phys. Rev. B* **76**, 024116 (2007).
- [67] J. Lüning, F. Nolting, A. Scholl, H. Ohldag, J. W. Seo, J. Fompeyrine, J.-P. Locquet, and J. Stöhr, Determination of the antiferromagnetic spin axis in epitaxial  $\text{LaFeO}_3$  films by x-ray magnetic linear dichroism spectroscopy, *Phys. Rev. B* **67**, 214433 (2003).
- [68] P. Kuiper, B. G. Searle, P. Rudolf, L. H. Tjeng, and C. T. Chen, X-ray magnetic dichroism of antiferromagnet  $\text{Fe}_2\text{O}_3$ : The orientation of magnetic moments observed by Fe  $2p$  x-ray absorption spectroscopy, *Phys. Rev. Lett.* **70**, 1549 (1993).